Dimerization activates the Inversin complex in *C. elegans*

Erika Beyrent[a,b], Derek T. Wei[a,b,†], Gwendolyn M. Beacham[a,b,†,‡], Sangwoo Park[c,e,§], Jian Zheng[a,‖], Matthew J. Paszek[c,d,e], and Gunther Hollopeter[a,b,*]

[a]Department of Molecular Medicine, Cornell University, Ithaca, NY 14853; [b]Field of Biochemistry, Molecular, and Cell Biology, Cornell University, Ithaca, NY 14853; [c]Field of Biophysics, Cornell University, Ithaca, NY 14853; [d]Robert Frederick Smith School of Chemical and Biomolecular Engineering, Cornell University, Ithaca, NY 14853; [e]Nancy E. and Peter C. Meinig School of Biomedical Engineering, Cornell University, Ithaca, NY 14853

ABSTRACT **Genetic, colocalization, and biochemical studies suggest that the ankyrin repeat-containing proteins Inversin (INVS) and ANKS6 function with the NEK8 kinase to control tissue patterning and maintain organ physiology. It is unknown whether these three proteins assemble into a static "Inversin complex" or one that adopts multiple bioactive forms. Through the characterization of hyperactive alleles in *C. elegans*, we discovered that the Inversin complex is activated by dimerization. Genome engineering of an RFP tag onto the nematode homologues of INVS (MLT-4) and NEK8 (NEKL-2) induced a gain-of-function, cyst-like phenotype that was suppressed by monomerization of the fluorescent tag. Stimulated dimerization of MLT-4 or NEKL-2 using optogenetics was sufficient to recapitulate the phenotype of a constitutively active Inversin complex. Further, dimerization of NEKL-2 bypassed a lethal MLT-4 mutant, demonstrating that the dimeric form is required for function. We propose that dynamic switching between at least two functionally distinct states – an active dimer and an inactive monomer – gates the output of the Inversin complex.**

SIGNIFICANCE STATEMENT

- Genetic and imaging data support the existence of an Inversin complex, but it has proven difficult to determine how the components act together to arrange organs and maintain tissue physiology.
- Using chemical mutagenesis, single-molecule imaging, and optogenetics in *C. elegans*, the authors find that inducing dimerization of the Inversin complex favors a constitutively active state required for viability. They propose the complex toggles between an inactive monomer and an active dimer.
- These findings present the first molecular mechanism for how the Inversin complex functions, offering a new route for determining its assembly, regulation, and potential downstream targets.

Monitoring Editor
Terry Lechler
Duke University

Received: May 20, 2024
Revised: Jul 25, 2024
Accepted: Aug 1, 2024

Cross-Validation

New Hypothesis

INTRODUCTION

Genetic data suggest that the ankyrin repeat-containing protein Inversin (INVS) functions with at least two other proteins, the never-in-mitosis A-related kinase 8 (NEK8) and the ankyrin repeat and sterile alpha motif-containing protein 6 (ANKS6). Loss of any one of the three proteins results in similar pathologies in humans and vertebrate models. INVS was initially identified at the genetic locus disrupted in mice that exhibit neonatal mortality with reversal of left-right asymmetry (*situs inversus*; Yokoyama *et al.*, 1993; Mochizuki *et al.*, 1998; Morgan *et al.*, 1998). INVS was later found to also be mutated in human patients presenting with infantile nephronophthisis – a disease characterized by *situs inversus* and end-stage renal failure, with cysts and fibrosis affecting multiple organs (Otto *et al.*, 2003; Zhong *et al.*, 2022). Two additional nephronophthisis loci have been identified as having mutations in NEK8 and ANKS6; vertebrate models confirm that loss of either of these proteins phenocopies loss of INVS (Otto *et al.*, 2008; Frank *et al.*, 2013; Hoff *et al.*, 2013; Taskiran *et al.*, 2014; Hassan *et al.*, 2020; Kulkarni *et al.*, 2020; Zhong *et al.*, 2022). In *C. elegans*, loss-of-function mutations in the INVS homolog, MLT-4, result in a lethal-molting phenotype, where worms fail to shed their collagen-based cuticles (Lažetić and Fay, 2017). Mirroring the genetic data from vertebrates, loss of NEKL-2 (NEK8) and MLT-2 (ANKS6) exhibit the same molting-defective phenotype (Yochem *et al.*, 2015; Lažetić and Fay, 2017). Thus, these three proteins appear to work together across multiple metazoan species.

Although loss-of-function experiments have been crucial in revealing the biological importance of INVS, NEK8, and ANKS6, it has proven difficult to determine the precise mechanisms by which these proteins are acting to control tissue patterning and maintain organ physiology. In *C. elegans*, all three proteins have been shown to function in endocytic trafficking to regulate molting (Joseph *et al.*, 2020, 2023). In vertebrates, a recent study proposed that INVS signals originating from the cilia counteract a cyst-activating pathway (Li *et al.*, 2023). Previous studies have implicated INVS in non-canonical *Wnt* signaling (Simons *et al.*, 2005; Jenny *et al.*, 2005; Feiguin *et al.*, 2001), while NEK8 and ANKS6 have been proposed to regulate Hippo signaling effectors (Grampa *et al.*, 2016; Airik *et al.*, 2020; Schwarz *et al.*, 2022). These mechanisms have been difficult to clarify, in part, due to a lack of gain-of-function analyses that could discriminate between direct actions of these proteins and indirect pathologies associated with loss-of-function lethality.

Cellular and biochemical data support the model that INVS, NEK8, and ANKS6 constitute an 'Inversin complex'; however, we lack fundamental knowledge about how the components might assemble into a functionally active state. Evidence from both vertebrates and invertebrates demonstrates the interdependence of the proteins for their localization. INVS appears to function as an anchor for the other two members in cilia, where the complex is observed to form a fibrillar structure by superresolution microscopy (Shiba *et al.*, 2010; Bennett *et al.*, 2020). Similar to the vertebrate proteins, the *C. elegans* homologues colocalize, albeit at epithelial junctions rather than cilia (Lažetić and Fay, 2017). While these localization patterns might not represent direct interactions, biochemical analyses have revealed the potential for the individual components to interact. For example, ANKS6 is reported to bind and stimulate the kinase activity of NEK8 (Czarnecki *et al.*, 2015; Nakajima *et al.*, 2018). It remains unclear whether the complex is a single static arrangement of the three proteins or undergoes dynamic switching between multiple states to specify its activity.

Here, we report that the Inversin complex is activated by dimerization. We identified an overt, morphological, cyst-like phenotype in *C. elegans* that signifies the complex is constitutively active. Tagging MLT-4 or NEKL-2 with a red fluorescent protein (RFP) induced this phenotype, and an unbiased genetic screen for phenotype suppression yielded monomerizing mutations in the fluorescent tag. We further demonstrate that optogenetic-induced dimerization is sufficient to generate the gain-of-function phenotype. Dimerization of the Inversin complex also appears to be required for function, as we can rescue a lethal MLT-4 mutant with dimerized NEKL-2. We propose that Inversin complex activity depends on switching between inactive monomeric and active dimeric states.

RESULTS

Jowls phenotype reports a constitutively active inversin complex

We reported previously that dominant, gain-of-function alleles of *mlt-4* cause a "jowls" phenotype in which fluid-filled pockets form at the anterior ends of *C. elegans* (Beacham *et al.*, 2022). The jowls phenotype is distinct from null mutants, which are lethal (Lažetić and Fay, 2017), and from hypomorphic mutants, which suppress jowls (Joseph *et al.*, 2020). One of our MLT-4 jowls alleles was a missense mutation isolated in a forward genetic screen (MLT-4 E470K; Figure 1, A and B), whereas a stronger allele resulted from attaching a tagRFP-T (henceforth referred to as "RFP tag") to the C-terminus of wild-type MLT-4 (MLT-4::RFP, Figure 1, A and B). In contrast to MLT-4 E470K, MLT-4::RFP animals exhibit a severe fitness deficit (Figure 1C; Beacham *et al.*, 2022) and are shorter or "dumpy" (Beacham *et al.*, 2022). However, they are scored as exhibiting a lower percentage of jowls compared with MLT-4 E470K animals (Figure 1B; Beacham *et al.*, 2022), suggesting that the MLT-4::RFP jowls phenotype may be partially masked by the dumpy phenotype. Curiously, the effect of the RFP tag appears to be specific, as no phenotype resulted from tagging MLT-4 with mScarlet, GFP, or HaloTag (Beacham *et al.*, 2022).

This article was published online ahead of print in MBoC in Press (http://www.molbiolcell.org/cgi/doi/10.1091/mbc.E24-05-0218) on Aug 7, 2024.

†These authors contributed equally.

‡Present address: Department of Medicine, Section of Hematology and Medical Oncology, Boston University Chobanian & Avedisian School of Medicine and Boston Medical Center, Boston, MA 02118; §Cellular Immunotherapy Program, Cancer Center, Massachusetts General Hospital and Harvard Medical School, Boston, MA 02114; ‖Molecular Biology Program, Memorial Sloan Kettering Cancer Center; and Programs in Biochemistry, Cell, and Molecular Biology, Weill Cornell Graduate School of Medical Sciences, New York, NY 10065.

Conflicts of interest: The authors declare no competing interest.

*Address correspondence to: Gunther Hollopeter (gh383@cornell.edu).

Abbreviations used: ANOVA, analysis of variance; ANKS6, ankyrin repeat and sterile alpha motif-containing protein 6; AJM-1, apical junction molecule 1; BSA, bovine serum albumin; CRISPR, clustered regularly interspaced short palindromic repeats; CV, coefficient of variance; DIC, differential interference contrast; DTT, dithiothreitol; ENU, n-nitroso-N-ethylurea; ER, endoplasmic reticulum; FP, fluorescent protein; GFP, green fluorescent protein; HRP, horseradish peroxidase; INVS, inversin; MLT-2, MoLTing defective 2; MLT-4, MoLTing defective 4; NGM, nematode growth medium; NEK8, never-in-mitosis A-related kinase 8; NEKL-2, never-in-mitosis A-related like kinase 2; n.s., not significant; OSER, organized smooth endoplasmic reticulum; PBS, phosphate-buffered saline; PCR, polymerase chain reaction; PDB, protein data bank; PEG, polyethylene glycol; PVDF, polyvinylidene difluoride; RFP, red fluorescent protein; RNP, ribonucleoprotein; RO, reverse osmosis; SDS-PAGE, sodium dodecyl sulfatepolyacrylamide gel electrophoresis; SD, standard deviation; TBS, tris-buffered saline; TBST, tris-buffered saline with 0.1% Tween-20; TIRF, total internal reflection fluorescence; WT, wild type.

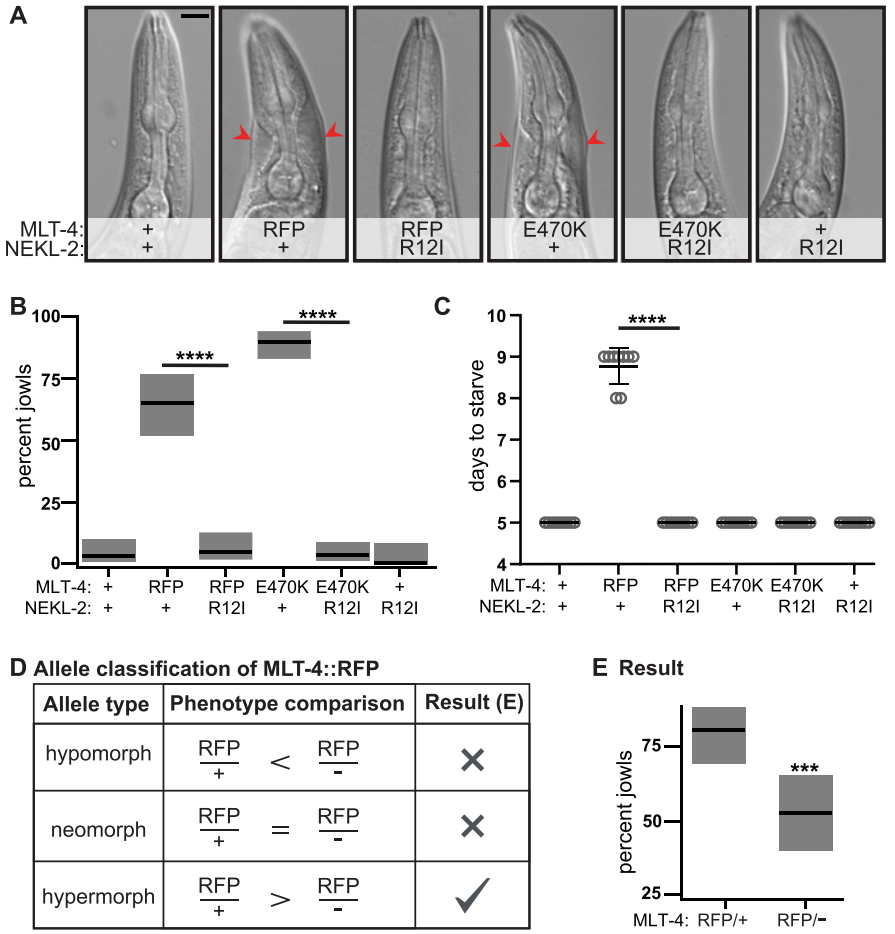

FIGURE 1: Hyperactive MLT-4 allele exhibits gain-of-function jowls phenotype. (A) Images of worm heads. Red arrows mark jowls. Scale bar = 20 μm. (B) Jowls assay. Percent of worms exhibiting jowls; gray boxes represent 95% confidence intervals. $n = 55–134$. (C) Fitness assay. Number of days for the population to expand and consume food source. Data represent the mean ± SD of 10 biological replicates. (D) Predicted penetrance of jowls for each allele class. (E) Results of allele classification. Percent of worms exhibiting jowls; gray boxes represent 95% confidence intervals. + = wild-type at indicated locus, − = *mlt-4* deletion allele. $n = 57–68$. *** $p < 0.001$, **** $p < 0.0001$, ANOVA analysis with Tukey's post hoc test, as indicated (B and C) or compared with RFP/+ (E).

We hypothesized that the RFP tag might stimulate the Inversin complex. To test this, we introduced a mutation into another member of the complex. The R12I mutation in NEK8 is associated with renal disease in humans and is hypothesized to reduce kinase activity (Hassan *et al.*, 2020). Indeed, engineering the analogous mutation in NEKL-2 suppressed the jowls phenotype of both MLT-4 alleles (Figure 1, A and B) and the fitness defect of MLT-4::RFP animals (Figure 1C). These results suggest that these MLT-4 alleles represent a gain-of-function that is dependent on NEKL-2.

Gain-of-function alleles can result from increased protein activity (hypermorphic) or a new, unrelated activity (neomorphic). To characterize the effect of the RFP tag, we generated heterozygous strains containing one copy of MLT-4::RFP and one copy of either a wild-type MLT-4 (referred to as MLT-4::RFP/+) or a deletion allele (referred to as MLT-4::RFP/–). In this scheme (Figure 1D), hypermorphic alleles will exhibit a *reduced* phenotype in the presence of a null allele, while the phenotype of hypomorphic alleles will be *enhanced* (Muller, 1932). Neomorphic alleles act independently and will exhibit the *same* phenotype regardless of the presence of a wild-type or null allele. We found that MLT-4::RFP/+ animals had an increased penetrance of jowls as compared with MLT-4::RFP/– animals (Figure 1E). This result is consistent with MLT-4::RFP being a hypermorphic allele.

To test whether an RFP tag also induces a hyperactive form of the kinase NEKL-2, we generated an inducible transgene of RFP-tagged NEKL-2 (RFP::NEKL-2; Supplemental Figure 1A). While expression of this transgene was lethal to larval animals, expression later in development induced jowls in adults (Supplemental Figure 1B). To test whether the jowls phenotype was dependent on the kinase activity of NEKL-2, we generated a kinase-dead version (D137N; Zalli *et al.*, 2012), and found that this mutation suppressed both the jowls phenotype and the fitness defect, as did the R12I disease allele (Supplemental Figure 1, B and C). Altogether, these results indicate that the jowls phenotype represents a biological output of a constitutively active Inversin complex.

Disruption of the RFP dimer interface suppresses jowls

To gain insight into how the RFP tag on MLT-4 acts as a hypermorphic allele, we conducted a chemical mutagenesis screen on the MLT-4::RFP strain for animals with suppressed jowls, and isolated

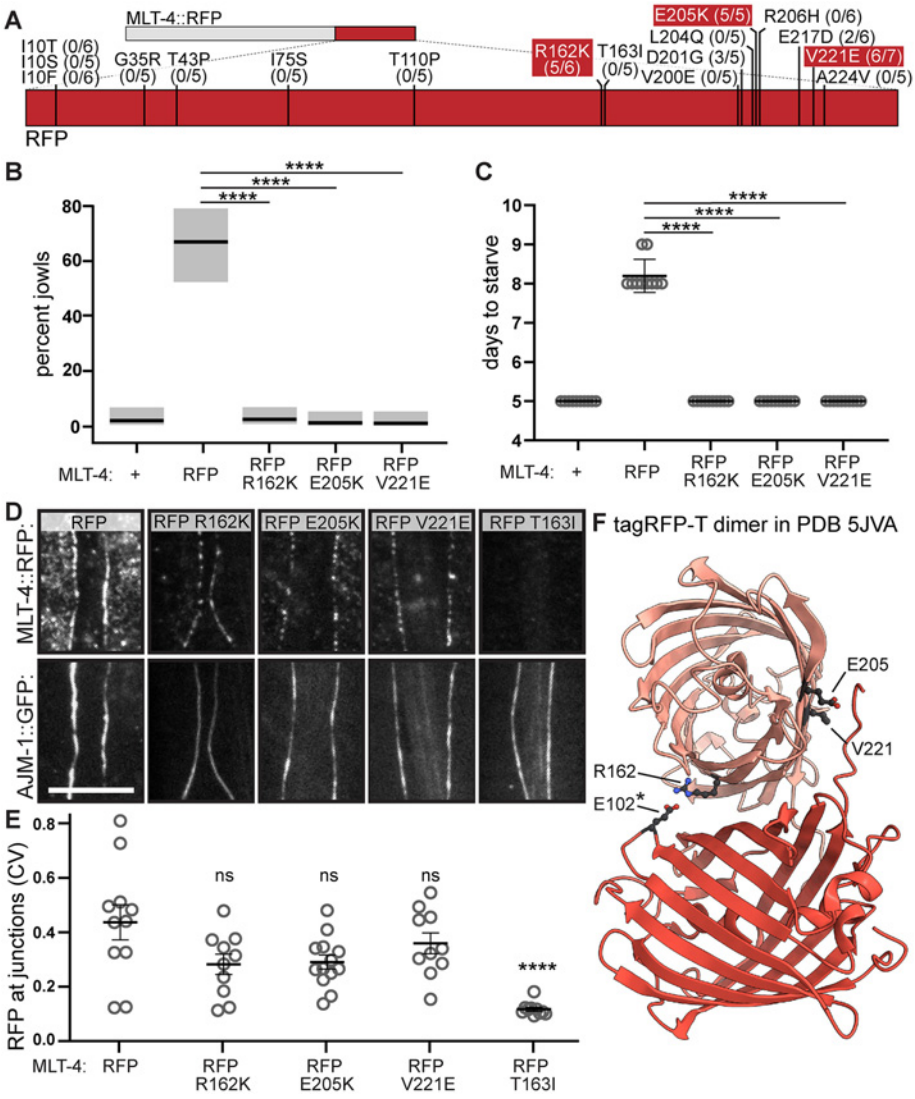

FIGURE 2: Characterization of missense mutations in RFP tag that suppress jowls. (A) Schematic of MLT-4::RFP. Fraction of worms exhibiting red fluorescence at epidermal junctions indicated for each mutant. Fluorescent mutants (red, >80%) were engineered de novo for B–E. (B) Jowls assay. Percent of worms exhibiting jowls; gray boxes represent 95% confidence intervals. $n = 46–138$. (C) Fitness assay. Number of days for the population to expand and consume food source. Data represents the mean ± SD of 10 biological replicates. (D) Imaging assay for MLT-4 localization at epithelial junctions. Representative images of endogenously tagged MLT-4::RFP (top) and apical junction marker AJM-1::GFP (bottom). Scale bar = 5 μm. (E) Quantification of MLT-4::RFP pixel intensity at junctions plotted as CV. Data represent mean ± SEM of 10–13 biological replicates. (F) Mutated residues mapped onto the structure of RFP tag (PDB 5JVA; note: residue numbers shifted - 5 in PDB). * Residue predicted to form a salt bridge; see Figure 3. For B and C, + = wild-type at mlt-4 locus. n.s. (not significant) $p > 0.05$, **** $p < 0.0001$, ANOVA analysis with Tukey's post hoc test, as indicated (B and C) or compared with RFP (E).

17 independent amino acid changes in the RFP tag (Figure 2A). We hypothesized that many of these mutations might destabilize the fluorophore and result in loss of fluorescence. Indeed, our screen selected a mutation in the key threonine residue (T163I) that is important for the photostability of tagRFP-T (Shaner *et al.*, 2008); the crystal structure (R. Liu *et al.*, 2016) shows this residue hydrogen bonding with the chromophore. As anticipated, our T163I mutant did not appear to be fluorescent (Figure 2, A, D, and E). Because it could be difficult to narrow down the precise molecular mechanism by which the other nonfluorescent RFP mutants suppress the jowls phenotype, we elected to focus on the missense mutants that retained red fluorescence in order to explore how fusing the RFP tag to MLT-4 causes jowls.

Three of the RFP missense mutants (R162K, E205K, and V221E) retained red fluorescence (Figure 2A). To confirm that these three mutations were indeed responsible for the suppression of the phenotype, we introduced them de novo using CRISPR. All three missense mutations suppressed both the jowls (Figure 2B) and the fitness defect (Figure 2C) of the MLT-4::RFP animals. We also confirmed that these MLT-4::RFP mutant proteins were appropriately localized to the apical junctions, which were demarcated by the apical epithelial junction marker AJM-1::GFP (Z. Liu *et al.*, 2005).

Although the red fluorescent signals appeared slightly reduced, all three retained a normal localization pattern (Figure 2, D and E), suggesting these mutations might have specifically disrupted a protein–protein interaction responsible for the jowls phenotype.

When we examined the positions of these mutated residues (R162, E205, and V221) on the crystal structure of tagRFP-T (R. Liu *et al.*, 2016), we observed that all three mapped to the dimer interface between two RFP molecules (Figure 2F). The residues analogous to E205 and V221 were previously modified to engineer monomeric forms of GFP (Zacharias *et al.*, 2002; Pédelacq *et al.*, 2006; Costantini *et al.*, 2012; Scott *et al.*, 2018). The other residue, R162, has previously been mutated to monomerize mKate (Shemiakina *et al.*, 2012) and mCardinal (Wannier *et al.*, 2018). To determine whether the R162K mutation isolated in our screen likewise favored MLT-4::RFP monomers, we employed single-molecule TIRF microscopy coupled with stepwise photobleaching. We lysed MLT-4::RFP worms and quantified the percentage of RFP-positive molecules within the lysate that exhibited a single photobleaching step. The R162K mutant consistently increased the monomeric fraction even as we increased the particle density (Figure 3A), consistent with an increase in RFP monomers.

In the crystal structure, R162 appears to bridge the dimer interface via an electrostatic interaction with residue E102 (Figure 2F). We hypothesized that mutating E102 in MLT-4::RFP animals should reduce dimerization and suppress jowls, similar to the mutation of R162. Indeed, an alanine mutant (E102A) suppressed both the jowls (Figure 3B) and fitness defect (Figure 3C) of MLT-4::RFP animals, without overtly perturbing the fluorescence or localization of MLT-4::RFP (Figure 3, D and E). Taken together, these data strongly suggest that the RFP tag forces dimerization of MLT-4 to generate a constitutively active Inversin complex.

Optogenetic dimerization of MLT-4 and NEKL-2 causes jowls

To test the differential effects of dimerization on Inversin complex subunits, we utilized the fungal photoreceptor Vivid, which has been shown to dimerize in a light-inducible manner (Shrode *et al.*, 2001; Zoltowski and Crane, 2008). We fused Vivid to each of the Inversin complex members using CRISPR, and induced dimerization of the Vivid tag with ambient light. When we attached Vivid to the C-terminus of either MLT-4 or NEKL-2, worms exposed to light exhibited jowls as adults, while worms grown in the dark did not (Figure 4, A–C). However, we did not see a robust fitness defect associated with fusing Vivid to NEKL-2 or MLT-4 (Figure 4D), in contrast to the RFP tags. Perhaps Vivid dimerization is not as robust as RFP at overcoming potential steric barriers or regulatory mechanisms that stabilize Inversin complex monomers, or it could be that the jowls and fitness defects are due to differential outputs of the Inversin complex. Interestingly, we failed to observe a phenotype when we fused Vivid to either the N- or C-terminus of MLT-2. These results could suggest that steric hindrance prevents Vivid-dependent dimerization of MLT-2, or that MLT-2 regulates the complex through a different mechanism. Altogether, these optogenetic studies show that dimerization of either MLT-4 or NEKL-2 is sufficient to activate the complex.

Dimerization of NEKL-2 rescues a functionally inactive MLT-4 mutant

Our screen for suppressors of the MLT-4::RFP phenotype also yielded mutations in MLT-4 itself (T94P, E291A, and N442K; Figure 5A). To determine whether any of these mutations specifically counteract dimerization, we followed the same strategy that we used to identify monomerizing mutants in the RFP tag. We engineered these MLT-4 mutations de novo to confirm that they suppressed MLT-4::RFP animals. While all three mutations fully suppressed the fitness defect caused by MLT-4::RFP (Figure 5B), only two (T94P and E291A) fully suppressed the jowls (Figure 5C). While the E291A mutant localized appropriately, both the N442K and T94P mutants exhibited significantly reduced fluorescent signals at the junctions (Figure 5, D and E). All three mutants appear to be stably expressed by Western blot analysis (Figure 5F), suggesting that N442K and T94P may result in diffuse mislocalization in the cytosol. Because the E291A mutation appeared to be a strong suppressor that is stably expressed and correctly localized, we hypothesized that E291A could be disrupting the dimerization of the complex and favoring a monomeric state.

If dimerization of the Inversin complex is required for its function, a monomerizing mutant should phenocopy a lethal null mutant in the absence of a dimerization tag (Figure 6A). To test this, we generated the E291A mutant in an untagged MLT-4 strain and compared the phenotype to that of a MLT-4 deletion. Because *mlt-4* nulls are lethal, we generated the MLT-4 deletion and the E291A mutation in worms rescued by extrachromosomal arrays of MLT-4. We then evaluated the phenotype of offspring that did not inherit the array. For both the homozygous MLT-4 null and E291A strains, 0% of the array-negative worms survived, compared with ∼95% of their array-positive siblings (Figure 6B).

We further reasoned that a monomerizing mutant should be rescued by inducing dimerization of the complex (Figure 6A), whereas a null would not. Presumably, dimerization of MLT-4 by the RFP tag enabled us to isolate the E291A mutation from our screen. To test whether dimerization of another member of the complex could similarly rescue the lethality of this mutant, we generated the E291A mutation in the NEKL-2::Vivid strain. We found that light-induced dimerization of NEKL-2 rescued E291A lethality (84% of offspring survived, Figure 6B). Importantly, a MLT-4 deletion was not rescued by dimerization of NEKL-2 (0% of offspring survived, Figure 6B), suggesting that the E291A mutation specifically counteracts dimerization of the Inversin complex.

DISCUSSION

Loss-of-function analyses and colocalization studies of Inversin complex proteins from both vertebrates and invertebrates show that INVS, NEK8, and ANKS6 work together, but how the activity of the Inversin complex is regulated to produce a functional output is largely unknown. Our results suggest that there are at least two functionally distinct states of the complex: an inactive monomer and an active dimer (Figure 6C). We hypothesize that the hyperactive jowl alleles stabilize the active dimer state; we can induce dimerization optogenetically and recapitulate the phenotype. We further hypothesize that a missense mutation isolated from our suppressor screen appears to favor the inactive monomer state; the lethality of the mutation is bypassed by forcing dimerization of NEKL-2. Thus, we propose dynamic switching between these two states as a new model for how the Inversin complex functions.

A new functional assay for Inversin complex activity

Previous work has shown that loss of the Inversin complex in *C. elegans* results in a lethal molting defect (Yochem *et al.*, 2015; Lažetić and Fay, 2017). In vertebrates, many of the nephronophthisis disease-associated mutations in INVS, ANKS6, and NEK8 result in early stops or frameshifts, suggesting that they also result in loss-of-function (Otto *et al.*, 2003; Frank *et al.*, 2013; Kulkarni *et al.* 2020).

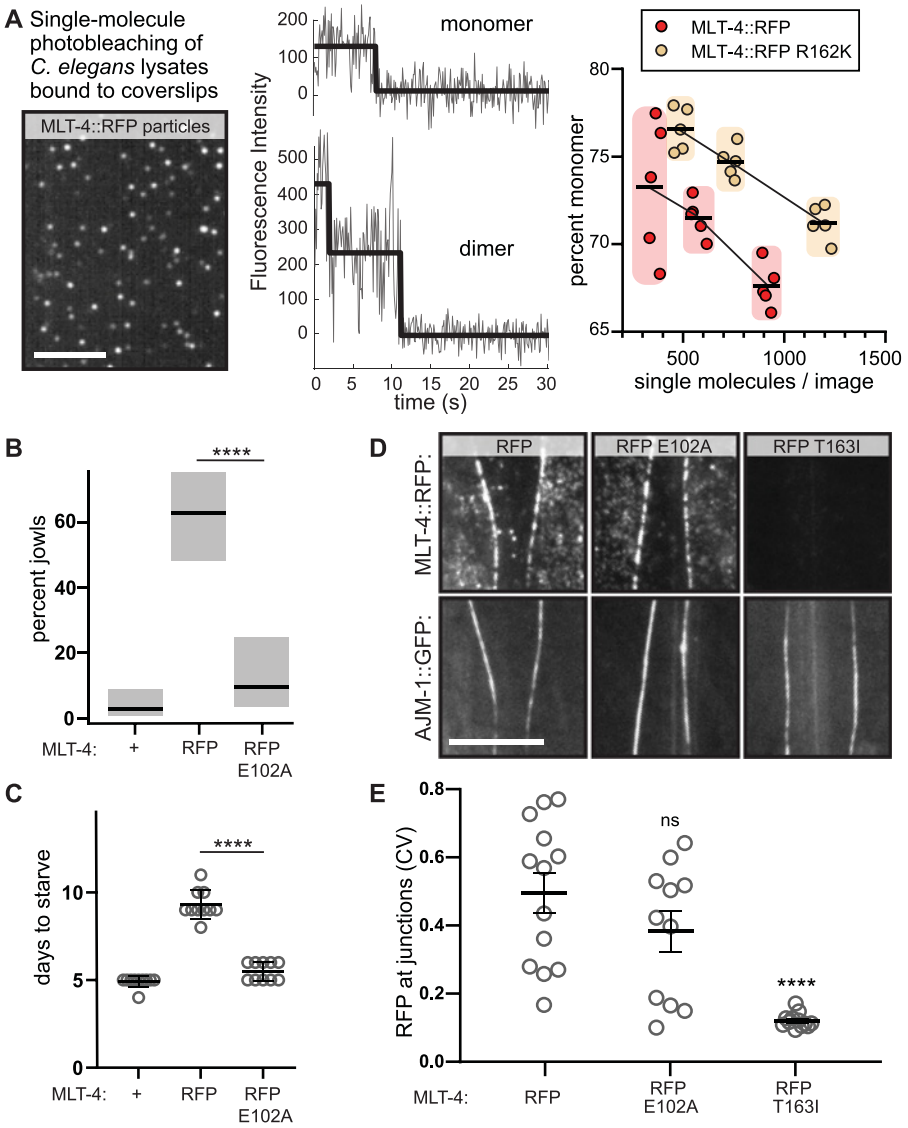

FIGURE 3: Perturbation of RFP dimerization reverses jowls phenotype. (A) Single-molecule photobleaching assay. Left: Representative TIRF image of MLT-4::RFP single molecules (average intensity projection of frames 6–50). Middle: Representative fluorescence intensity traces of MLT-4::RFP monomer (top) and dimer (bottom). Right: Percent of MLT-4::RFP spots exhibiting a single bleaching step. Data collected from five to eight images (circles) across three comparable particle densities (shaded clusters, mean indicated). (B) Jowls assay. Percent of worms exhibiting jowls; gray boxes represent 95% confidence intervals. $n = 35–92$. (C) Fitness assay. Number of days for the population to expand and consume food sources. Data represent the mean ± SD of 10 biological replicates. (D) Imaging assay for MLT-4 localization at epithelial junctions. Representative images of endogenously tagged MLT-4::RFP (top) and apical junction marker AJM-1::GFP (bottom). (E) Quantification of MLT-4::RFP pixel intensity at junctions plotted as CV. Data represent the mean ± SEM of 11–13 biological replicates. + = wild-type at *mlt-4* locus. n.s. $p > 0.05$, **** $p < 0.0001$, ANOVA analysis with Tukey's post hoc test, as indicated (B and C) or compared with RFP (E). All scale bars = 5 μm.

Despite the characterization of how these loss-of-function alleles affect localization, ciliogenesis, and cyst formation (Otto *et al.*, 2008; Zalli *et al.*, 2012), we lack a comprehensive understanding of the normal activity of the complex due to the absence of gain-of-function analyses, which could identify potential downstream targets. In this paper, we conclude that the MLT-4::RFP allele is likely hyperactive because it is dominant and modulated by the dosage of the wild-type gene (Figure 1, D and E). This allele enabled us to characterize a recessive point mutation in the NEK8 kinase domain (R12I) associated with end-stage renal failure (Hassan *et al.*, 2020). In our animals, the R12I disease allele suppressed the gain-of-function jowls phenotype, but is not lethal (Figure 1, A and C). These results are consistent with the R12I mutation being a hypomorphic allele, as opposed to a loss-of-function allele. Thus, our jowls assay can be used to assess additional disease-associated missense mutations as they are discovered.

Our results show that constitutive dimerization of MLT-4 or NEKL-2 causes jowls. Although we looked specifically at dimerization in this paper, we cannot rule out that a higher-order oligomer is the true active state. Indeed, superresolution microscopy data suggest that the Inversin complex forms fibril-like structures in cilia (Bennett *et al.*, 2020), but the functional significance of these

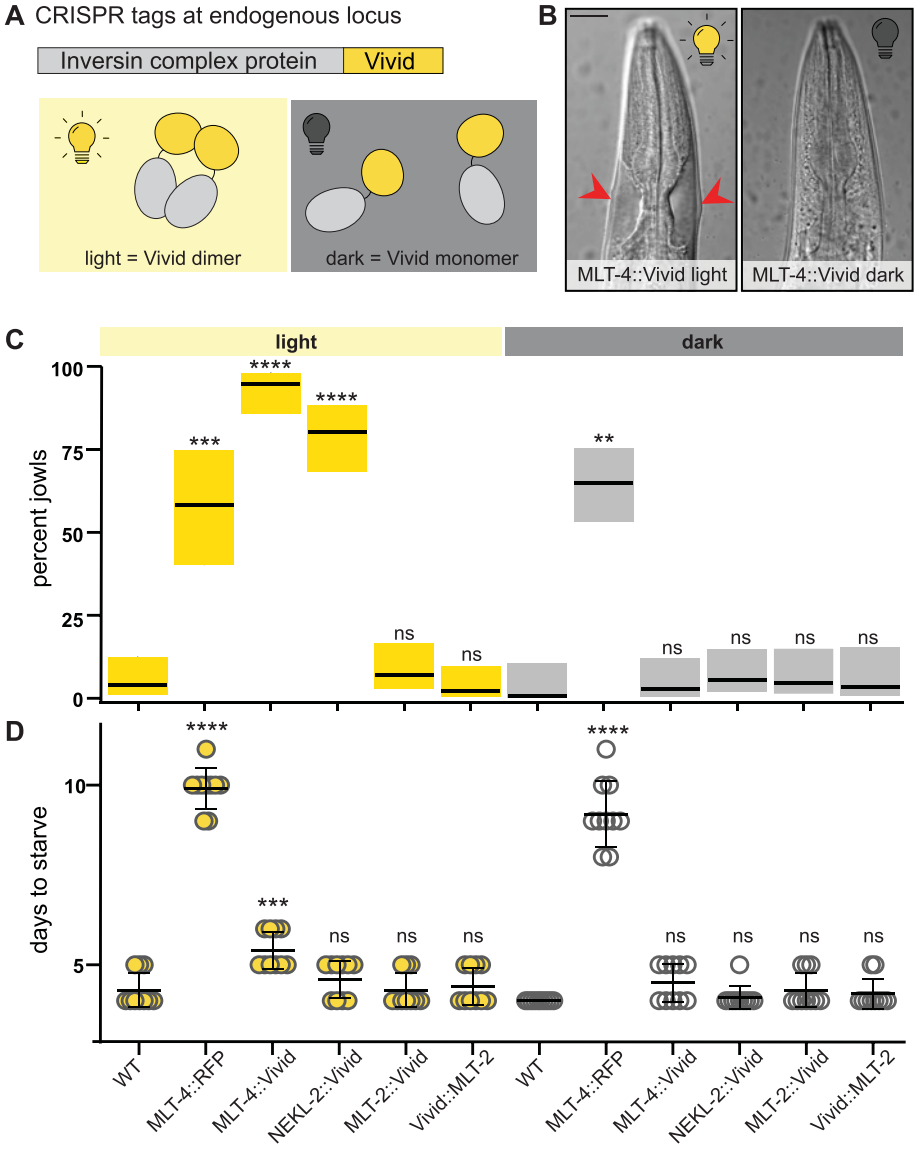

FIGURE 4: Optogenetic dimerization of MLT-4 or NEKL-2 causes jowls. (A) Diagram of light-dependent dimerization of Vivid tag fused to Inversin complex protein. (B) Images of worm heads. Red arrows indicate jowls. Scale bar = 20 μm. (C) Jowls assay. Percent of worms exhibiting jowls; gray boxes represent 95% confidence intervals. $n = 29–72$. (D) Fitness assay. Number of days for the population to expand and consume food sources. Data represent the mean ± SD of 10 biological replicates. WT = wild-type Bristol N2. n.s. $p > 0.05$,** $p < 0.01$, *** $p < 0.001$, **** $p < 0.0001$, ANOVA analysis with Tukey's post hoc test, compared with + within respective light/dark conditions.

structures remains unclear. Interestingly, we did not observe jowls when we attempted to dimerize MLT-2 by fusing Vivid to either terminus (Figure 4). Several studies in both *C. elegans* and vertebrates suggest that MLT-2/ANKS6 is part of the same complex as NEKL-2/NEK8 and MLT-4/INVS, and is required for activation of the kinase (Hoff *et al.*, 2013; Czarnecki *et al.* 2015; Lažetić *et al.*, 2018). The simplest explanation for our result is that steric hindrance prevents dimerization of MLT-2 when fused to Vivid. Alternatively, MLT-2 could be functioning differently from MLT-4 and NEKL-2 in our animals to regulate the complex through a mechanism independent of dimerization. Differential impact of dimerization on the individual subunits could also point to the hierarchical assembly of Inversin complex components that can be explored in future studies.

Why does the Inversin complex require dimerization to be active? NEK8 is thought to act downstream of INVS (Fukui *et al.*, 2012), and many kinases are known to become active via autophosphorylation in response to dimerization (Hubbard and Miller, 2007). A previous study suggests that NEK8 activity is dependent on autophosphorylation (Zalli *et al.*, 2012). Our results support a model whereby dimerization could promote autophosphorylation. However, if the kinase were strictly downstream of INVS, then dimerization of the kinase with Vivid should bypass a MLT-4 deletion – it does not (Figure 6B). Instead, this result is consistent with data from multiple systems showing that MLT-4/INVS, along with MLT-2/ANKS6, is required for the localization of NEKL-2/NEK8 (Hoff *et al.*, 2013; Lažetić and Fay, 2017; Bennett *et al.*, 2020). Indeed, we find that a properly localized, yet lethal, MLT-4 mutant (E291A) is rescued by dimerization of NEKL-2 (Figure 6B). However, the animals did not exhibit jowls, indicating that the E291A mutant reduces dimerization of the kinase. Altogether,

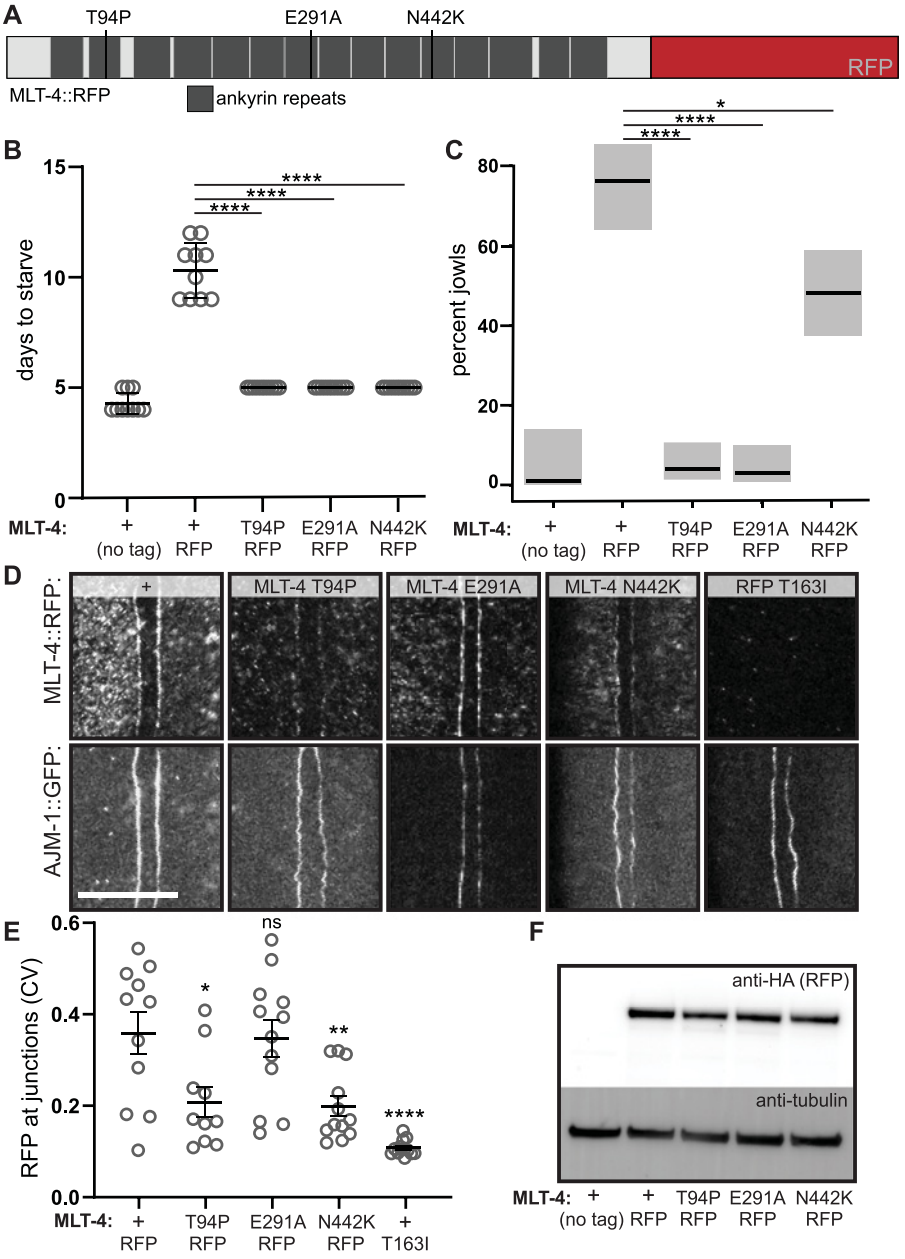

FIGURE 5: Characterization of missense mutations in MLT-4 that suppress jowls. (A) Schematic of MLT-4::RFP indicating mutations in MLT-4 isolated from mutagenesis screen. (B) Jowls assay. Percent of worms exhibiting jowls; gray boxes represent 95% confidence intervals. $n = 51–88$. (C) Fitness assay. Number of days for the population to expand and consume food sources. Data represent means ± SD of 10 biological replicates. (D) Imaging assay for MLT-4 localization at epithelial junctions. Representative images of endogenously tagged MLT-4::RFP (top) and apical junction marker AJM-1::GFP (bottom). Scale bar = 5 μm. (E) Quantification of MLT-4::RFP pixel intensity at junctions plotted as CV. Data represent means ± SEM of 10–12 biological replicates. (F) Western blot dual-labeled for HA tag on MLT-4::RFP (top) and loading control (bottom). + = wild-type at *mlt-4* locus. n.s. $p > 0.05$, * $p \leq 0.05$, ** $p < 0.01$, *** $p < 0.001$, **** < 0.0001, ANOVA analysis with Tukey's post hoc test, as indicated (B and C) or compared with MLT-4::RFP (E).

these results suggest that the Inversin complex proteins are acting as interdependent subunits.

An in vivo strategy to assess the monomeric character of fluorescent proteins and other genetically encodable tags

Most genetically encodable fluorophores descend from dimeric or tetrameric proteins. Thus, a central focus of fluorescent protein (FP) engineering is generating monomeric versions. The standard in vitro assays for determining the oligomeric state of FPs include gel filtration, ultracentrifugation, and structural analyses. However, the propensity of an FP to dimerize often depends on its cellular environment. Currently, the standard in vivo assay of FP oligomerization is the OSER assay, which assesses FPs fused to ER-membrane proteins. If the FP oligomerizes, it will deform the ER and create whorl-like structures (Snapp *et al.*, 2003). Using this assay, TagRFP has been shown to dimerize in cells (Costantini *et al.*, 2012), even

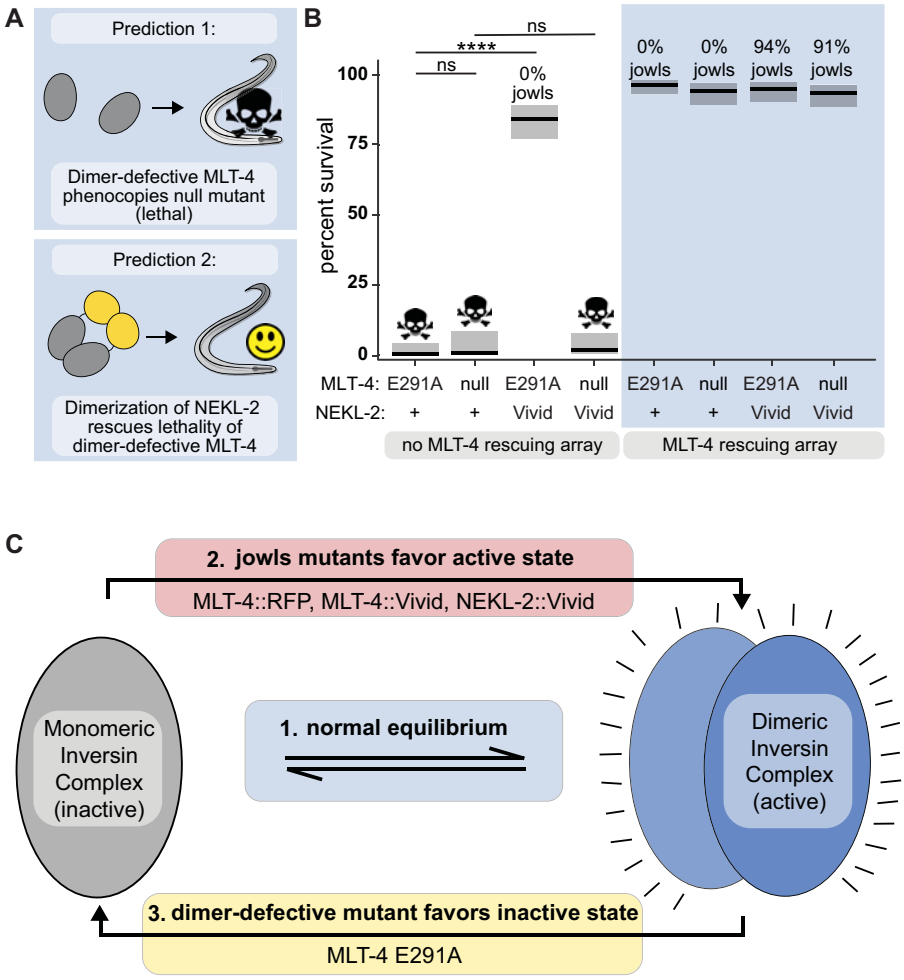

FIGURE 6: Dimerization of NEKL-2 rescues a functionally inactive MLT-4 mutant. (A) Graphic summary of phenotype predictions for a dimer-defective Inversin complex mutation. (B) Percent of worms surviving to adulthood; gray boxes represent 95% confidence intervals. $n = 89–271$. Percent jowls are indicated for the strains that were viable. (C) Model for dimerization-dependent activation of the Inversin complex. + = wild-type at *nekl-2* locus. n.s. $p > 0.05$, ** $p < 0.01$, *** $p < 0.001$, **** $p < 0.0001$, ANOVA analysis with Tukey's post hoc test, as indicated.

though it appears monomeric in vitro (Merzlyak *et al.*, 2007). Our results are consistent with tagRFP-T having a propensity to dimerize in vivo (Figures 2, 3, and 4). We previously found that tagging MLT-4 with mScarlet does not cause jowls (Beacham *et al.*, 2022), which is also consistent with results from the OSER assay where mScarlet exhibited 75% normal cells (Bindels *et al.*, 2017).

Interestingly, our suppressor screen generated mutations in tagRFP-T that have previously been shown to monomerize FPs. Two of the residues mutated in our screen that retain red fluorescence (E205 and V221, Figure 2A) have been previously shown to be important for the monomerization of GFP according to both in vitro methods and the OSER assay (Zacharias *et al.*, 2002; Pédelacq *et al.*, 2006; Costantini *et al.*, 2012; Scott *et al.*, 2018). The R162 residue in tagRFP-T arose in tagRFP from random mutagenesis, and then later was mutated to reduce dimerization in the development of mKelly2 (Wannier *et al.*, 2018) and fusionRed (Shemiakina *et al.*, 2012). Several other residues that were identified in our suppressor screen as nonfluorescent mutants have also been modified to monomerize other FPs. For example, T110 was mutated to a proline in our screen but to a lysine in order to generate mCarmine (Fabritius *et al.*, 2018). Similarly, V200E was isolated in our screen but was mutated to isoleucine in the development of mMaroon (Bajar *et al.*, 2016). Although these particular mutations (T110P and V200E) resulted in a loss of fluorescence in our screen, it is possible that they disrupt dimerization by destabilizing the fluorophore. Our results suggest a novel strategy to evaluate the monomeric nature of any FP or other genetically encodable tags in vivo.

MATERIALS AND METHODS

Worm strains, maintenance, and CRISPR-Cas9 transgenics

Strains were maintained at room temperature (or 15°C for Figure 2A) on nematode growth medium (NGM) plates seeded with a bacterial food source (strain OP50). CRISPR-Cas9 edits were generated by injecting *C. elegans* gonads with ribonucleoprotein (RNP) complexes as described in (Ghanta and Mello, 2020), using unmodified oligonucleotides and slight modifications to the annealing strategy as described in (Beacham *et al.*, 2022). For a complete list of components of the RNP complexes, including crRNAs, accompanying repair strategies, and resulting strains and alleles, see Supplemental File 1. Alleles generated by CRISPR were confirmed by sequencing a PCR amplicon of the modified locus.

MLT-4::RFP suppressor screen

MLT-4::RFP mutants (GUN405) were mutagenized as described in (Beacham *et al.*, 2022). Briefly, worms were incubated for 4 h at 22°C in 0.5 mM N-nitroso-N-ethylurea (ENU, Sigma Aldrich N3385), washed thoroughly in M9 buffer (22 mM KH_2HPO_4, 42.3 mM Na_2HPO_4, 85.6 mM NaCl, 1 mM $MgSO_4$), distributed across NGM growth plates seeded with concentrated OP50 bacterial culture, and passaged several times to select for worms with increased fitness. One suppressed animal per culture plate was selected to ensure the isolation of independent suppressors. Genomic regions corresponding to the RFP tag and *mlt-4* gene were amplified and sequenced to identify mutations.

DIC and live fluorescent imaging

For DIC imaging, worms were mounted on 2% agarose pads on glass slides in 20% sodium azide and imaged using a 40x DIC objective 10–20 min after overlay of a No. 1.5 glass coverslip. For fluorescent imaging, adult worms were mounted on 8–10% agarose pads on glass slides and immobilized using 0.1 μm polystyrene beads (Polysciences, Warrington, PA, 2.5% by volume) diluted 2-fold in PBS (pH 7.4) followed by an overlay of a No. 1.5 glass coverslip (Kim *et al.*, 2013). For the initial screening of fluorescent signal in the RFP tag mutants (Figure 2A), the focal planes between the alae and gonad were identified using brightfield microscopy. Then, a Z-stack of the red fluorescent channel was collected using a 60x oil immersion objective on a BZ-X810 Keyence microscope. Worms exhibiting fluorescent signals at epidermal junctions were scored for each strain. For quantification of junctional fluorescent signal (Figures 2, 3, and 5), Z-stacks flanking the AJM-1::GFP junctional marker were collected in both the green and red channels using a custom-built RM21 TIRF microscope (MadCity Labs) equipped with a 60x oil immersion TIRF objective (Nikon), 488- and 552 nm lasers (Coherent OBIS), and an Orca Fusion BT sCMOS camera (Hamamatsu). For image analysis, the AJM-1::GFP signal was used to select the single focal plane corresponding to the apical junctions. A segmented line (5 pixels wide) was drawn along the AJM-1::GFP signal and transformed into the red channel using Fiji (Schindelin *et al.*, 2012). The mean pixel intensity and standard deviation (SD) were measured to calculate the coefficient of variance (CV = SD/mean) for each segmented line in the red channel only.

Jowls assays

Synchronized populations of adult worms were scored for the presence of jowls under a dissecting microscope (Nikon SMZ800N). For allele classification in Figure 1E, MLT-4::RFP/– was generated by CRISPR as indicated in Supplemental File 1, resulting in a balanced heterozygous strain (GUN2180). MLT-4::RFP/+ heterozygous worms were generated by crossing N2 males with GUN350 hermaphrodites and selecting F1 animals. Offspring of MLT-4::RFP/+ and MLT-4::RFP/– heterozygotes were scored for jowls and genotyped *post hoc*. Only the confirmed heterozygous offspring were included in the analysis. For phenotypic analysis following induction of RFP::NEKL-2 expression in Supplemental Figure 1, jowls were scored 6 h post heatshock (34°C, 1 h).

Starvation assays

Three L4 worms were placed on each of 10 culture plates per strain and allowed to reproduce and expand. Plates were evaluated daily and marked as starved when all food was consumed.

Statistical analysis

Jowls assay and the survival assay in Figure 6 was analyzed in RStudio as described previously (Beacham *et al.*, 2022). Briefly, generalized linear models were fit to a binomial distribution. Starvation assays and imaging assays were analyzed in GraphPad. For all statistical comparisons, ANOVA analysis was performed using Tukey's method to adjust for multiple comparisons.

Western blot analysis

For each sample, 100 L4 worms were lysed in PBS with 1x Bolt LDS Sample Buffer (Invitrogen) containing 0.01% Triton X-100 and 25 mM DTT. Samples were frozen in liquid nitrogen before sonicating at 70% power for 3 min total (1 s on, 1 s off) in a cup horn sonicator. Samples were then incubated at 70°C for 10 min. Sonication and heating steps were repeated two to three times to ensure complete lysis. SDS–PAGE was performed using Bolt 4–12% Bis-Tris Plus precast gels (Invitrogen). Proteins were transferred to PVDF Immobilon-FL membranes (Merck Millipore) using the Power Blotter Semi-dry Transfer System (Thermo Fisher Scientific) according to product instructions. After transferring, membranes were blocked using EveryBlot Blocking Buffer (Biorad) for 10 min. Membranes were incubated in primary antibody diluted in blocking buffer [rat anti-HA HRP 1:500 (Roche 12013819001), mouse anti-tubulin 1:1000 (Sigma, T5168)] for 1 h at room temperature with orbital shaking, washed three times in TBST for 5 min each, and incubated in secondary antibody diluted in blocking buffer [goat anti-mouse 488 1:4000 (Thermo Fisher Scientific A11029)] for 30 min at room temperature with orbital shaking. Before imaging, membranes were washed three to four times in TBST for at least 5 min each. HRP was detected using SuperSignal West Dura Extended Duration Substrate (Thermo Fisher Scientific). Blots were imaged using the BioRad ChemiDoc MP imaging system, and band intensities were quantified using ImageLab software.

Molecular visualization

The structural representation of the tagRFP-T dimer (chains A and B of PDB 5JVA) in Figure 2F was prepared in ChimeraX (Goddard *et al.*, 2018; Pettersen *et al.*, 2021).

TIRF single molecule imaging

Coverslip PEGylation. Glass coverslips were placed in a glass Coplin jar containing acetone and sonicated using a water bath sonicator for 10 min. Coverslips were then rinsed five times with reverse osmosis (RO) water, sonicated in methanol for 10 min, washed five times with RO water, sonicated in 3N KOH for 40 min, washed five times with RO water, and rinsed in methanol. After drying, the coverslips were PEGylated by incubating in a 1:100 mixture of 1% biotin-PEG-silane in ethanol (Laysan Bio Biotin-PEG-SIL-2K-1g) and PEG-silane (85%, VWR 77035-498) for 1 h in the dark at room temperature. Coverslips were rinsed thoroughly in RO water and dried with nitrogen gas before storing them in the dark at room temperature in a Tupperware container with Drierite desiccant (VWR).

C. elegans lysate preparation. Worms were cultured at room temperature on 15 cm NGM plates seeded with concentrated OP50 *E. coli* culture mixed with chicken egg. When plates were confluent but not yet starved, worms were harvested using TBS and centrifuged at 180 × g at 4°C for 2 min. The supernatant was removed, and the pelleted worms were washed two times with TBS. Worms were resuspended in an equal volume of 2x lysis buffer (2x TBS, 0.2% TX-100, and 10% glycerol with protease

inhibitors [Roche, 1 tablet per 25 ml lysis buffer]). The resulting worm slurry was frozen dropwise in liquid nitrogen and stored at −80°C until lysis. Frozen worm pellets were ground in a coffee grinder prechilled with liquid nitrogen. When the ground sample lacked intact worms, as verified by thawing an aliquot on a slide under a dissecting scope, the remaining powdered sample was stored at −80°C. Immediately before slide preparation for imaging, an aliquot was thawed on ice and spun at 17,000 × g for 2 min at room temperature. The supernatant was collected and applied to PEGylated coverslips for imaging (described below).

Slide preparation for imaging. Before imaging, multichannel devices were assembled by adhering a coated coverslip to an uncoated glass slide using ∼4 mm strips of double-sided tape placed orthogonally to the long axis. Each channel was filled by capillary action with wash buffer (10 mM Tris, pH 8.0, 50 mM NaCl, 0.01% BSA, 0.01% TX-100). Channels were washed two times before each of the following steps: 10-min incubation with 0.2 mg/ml neutravidin (Thermo Fisher Scientific) in wash buffer, 10-min incubation with biotinylated antibody [anti-HA biotin (Roche 12158167001) diluted 1:100 in wash buffer], 10-min incubation with blocking buffer (10 mM Tris, pH 8.0, 50 mM NaCl, 2% BSA, 0.01% TX-100), and 15-min incubation with *C. elegans* lysate. Channels were washed three times before imaging. Samples were imaged using an RM21 TIRF microscope (MadCity Labs) equipped with a 60x oil immersion TIRF objective (Nikon), a 552-nm laser (Coherent OBIS), and an Orca Fusion BT sCMOS camera (Hamamatsu).

Data analysis. Single-molecule detection and analysis of photobleaching steps were performed automatically using SimPull Analysis Software https://github.com/dickinson-lab/SiMPull-Analysis-Software (Dickinson *et al.*, 2017; Stolpner and Dickinson, 2022). Samples were excluded if particle densities precluded accurate single-molecule spot detection. Single molecules that were rejected by the SimPull Analysis Software (molecules that did not photobleach or molecules that exhibited an increase in intensity over the course of imaging) were excluded from the final analysis.

Vivid transgenes and light exposure

The sequence of *Neurospora crassa* Vivid (Uniprot entry Q1K5Y8_NEUCR) was synthesized as a gBlock (IDT) with the following modifications: the first 36 amino acids were removed (Zoltowski and Crane, 2008; Vaidya *et al.*, 2011), a point mutation (I52C) that has previously been shown to stabilize the dimer state was introduced (Nihongaki *et al.*, 2014), and a *C. elegans* intron was added using *C. elegans* Codon Adapter (Redemann *et al.*, 2011). The resulting synthetic gene (gbEB3) was amplified for CRISPR repairs. Although Vivid is most sensitive to blue light, culture plates were exposed to ambient light because long-term exposure to blue light induces *C. elegans* embryonic lethality.

Array rescue experiments

Homozygous MLT-4 null and MLT-4 E291A worm strains rescued by MLT-4 extrachromosomal arrays (GUN2409 and GUN2407, respectively) were generated by injecting a MLT-4::GFP plasmid (along with neuronal marker pGH5) into MLT-4::RFP/MLT-4 null and MLT-4::RFP/MLT-4 E291A heterozygotes. Array-rescued MLT-4 null or E291A homozygous candidates (array-positive offspring lacking jowls) were isolated and confirmed by genotyping. The NEKL-2::Vivid; MLT-4 null strain rescued by an MLT-4 array (GUN2413) was generated by crossing heterozygous NEKL-2::Vivid males with GUN2409. The NEKL-2::Vivid; MLT-4 E291A strain (GUN2411) was generated by CRISPR, as indicated in Supplemental File 1. For the survival assay in Figure 6, 6-h broods were collected from array-positive adults. Upon hatching, siblings were separated into array-positive and array-negative pools and scored for viability once the array-positive cohort reached adulthood.

ACKNOWLEDGMENTS

We thank the Cornell statistical consulting unit; Kelly Liu for sharing strains; Eric Drier for advice on classification of alleles; Ed Partlow, Chun Han, and Justin Taraska for advice regarding the RFP mutations; Dan Dickinson, Jeff Lange, and Kevin Cannon for advice on single-molecule experiments; Maria Henriquez, Jenna Benton, Kayleigh Morrison, and Mari Camacho for technical support. We also thank the labs of Maurine Linder, Carrie Adler, Josh Chappie, and Rick Cerione for sharing space and reagents, as well as Rick Baker, Kayleigh Morrison, Justin Tapper, and Carrie Adler for constructive criticism that greatly improved the manuscript. This work was supported by a grant from the National Institutes of Health (R01 GM127548) awarded to Gunther Hollopeter.

REFERENCES

Airik M, Schüler M, McCourt B, Weiss A-C, Herdman N, Lüdtke TH, Widmeier E, Stolz DB, Nejak-Bowen KN, Yimlamai D, *et al.* (2020). Loss of Anks6 Leads to YAP Deficiency and Liver Abnormalities. Hum Mol Gen 29, 3064–3080.

Bajar BT, Lam AJ, Badiee RK, Oh Y-H, Chu J, Zhou XX, Kim N, Kim BB, Chung M, Yablonovitch AL, *et al.* (2016). Fluorescent Indicators for Simultaneous Reporting of All Four Cell Cycle Phases. Nat Methods 13, 993–996.

Beacham GM, Wei DT, Beyrent E, Zhang Y, Zheng J, Camacho MMK, Florens L, Hollopeter G (2022). The Caenorhabditis Elegans ASPP Homolog APE-1 Is a Junctional Protein Phosphatase 1 Modulator. Genetics 222.

Bennett HW, Gustavsson A-K, Bayas CA, Petrov PN, Mooney N, Moerner WE, Jackson PK (2020). Novel Fibrillar Structure in the Inversin Compartment of Primary Cilia Revealed by 3D Single-Molecule Superresolution Microscopy. Mol Biol Cell 31, 619–639.

Bindels DS, Haarbosch L, van Weeren L, Postma M, Wiese KE, Mastop M, Aumonier S, Gotthard G, Royant A, Hink MA, *et al.* (2017). mScarlet: A Bright Monomeric Red Fluorescent Protein for Cellular Imaging. Nat Methods 14, 53–56.

Costantini LM, Fossati M, Francolini M, Snapp EL (2012). Assessing the Tendency of Fluorescent Proteins to Oligomerize under Physiologic Conditions. Traffic 13, 643–649.

Czarnecki PG, Gabriel GC, Manning DK, Sergeev M, Lemke K, Klena NT, Liu X, Chen Y, Li Y, San Agustin JT, *et al.* (2015). ANKS6 Is the Critical Activator of NEK8 Kinase in Embryonic Situs Determination and Organ Patterning. Nat Commun 6, 6023.

Dickinson DJ, Schwager F, Pintard L, Gotta M, Goldstein B (2017). A Single-Cell Biochemistry Approach Reveals PAR Complex Dynamics during Cell Polarization. Dev Cell 42, 416–434.e11.

Fabritius A, Ng D, Kist AM, Erdogan M, Portugues R, Griesbeck O (2018). Imaging-Based Screening Platform Assists Protein Engineering. Cell Chem Biol 25 , 1554–1561.e8.

Feiguin F, Hannus M, Mlodzik M, Eaton S (2001). The Ankyrin Repeat Protein Diego Mediates Frizzled-Dependent Planar Polarization. Dev Cell 1, 93–101.

Frank V, Habbig S, Bartram MP, Eisenberger T, Veenstra-Knol HE, Decker C, Boorsma RAC, Göbel H, Nürnberg G, Griessmann A, *et al.* (2013). Mutations in NEK8 Link Multiple Organ Dysplasia with Altered Hippo Signalling and Increased c-MYC Expression. Hum Mol Gen 22, 2177–2185.

Fukui H, Shiba D, Asakawa K, Kawakami K, Yokoyama T (2012). The Ciliary Protein Nek8/Nphp9 Acts Downstream of Inv/Nphp2 during Pronephros Morphogenesis and Left–right Establishment in Zebrafish. FEBS Letters 586, 2273–2279.

Ghanta KS, Mello CC (2020). Melting dsDNA Donor Molecules Greatly Improves Precision Genome Editing in Caenorhabditis Elegans. Genetics 216, 643–650.

Goddard TD, Huang CC, Meng EC, Pettersen EF, Couch GS, Morris JH, Ferrin TE (2018). UCSF ChimeraX: Meeting Modern Challenges in Visualization and Analysis. Protein Sci 27, 14–25.
Grampa V, Delous M, Zaidan M, Odye G, Thomas S, Elkhartoufi N, Filhol E, Niel O, Silbermann F, Lebreton C, *et al.* (2016). Novel NEK8 Mutations Cause Severe Syndromic Renal Cystic Dysplasia through YAP Dysregulation. PLoS Genetics 12, e1005894.
Hassan S, Wolf MTF, Umaña LA, Malik S, Uddin N, Andersen J, Aqul A (2020). Homozygous NEK8 Mutations in Siblings With Neonatal Cholestasis Progressing to End-Stage Liver, Renal, and Cardiac Disease. J Pediatr Gastroenterol Nutr 70, e19.
Hoff S, Halbritter J, Epting D, Frank V, Nguyen T-MT, Reeuwijk J, Boehlke C, Schell C, Yasunaga T, Helmstädter M, *et al.* (2013). ANKS6 Is a Central Component of a Nephronophthisis Module Linking NEK8 to INVS and NPHP3. Nat Genet 45, 951–956.
Hubbard SR, Miller WT (2007). Receptor Tyrosine Kinases: Mechanisms of Activation and Signaling. Curr Opin Cell Biol 19, 117–123.
Jenny A, Reynolds-Kenneally J, Das G, Burnett M, Mlodzik M (2005). Diego and Prickle Regulate Frizzled Planar Cell Polarity Signalling by Competing for Dishevelled Binding. Nat Cell Biology 7, 691–697.
Joseph BB, Wang Y, Edeen P, Lažetić V, Grant BD, Fay DS (2020). Control of Clathrin-Mediated Endocytosis by NIMA Family Kinases. PLoS Genetics 16, e1008633.
Joseph BB, Naslavsky N, Binti S, Conquest S, Robison L, Bai G, Homer RO, Grant BD, Caplan S, Fay DS (2023). Conserved NIMA Kinases Regulate Multiple Steps of Endocytic Trafficking. PLoS Genetics 19, e1010741.
Kim E, Sun L, Gabel CV, Fang-Yen C (2013). Long-Term Imaging of Caenorhabditis Elegans Using Nanoparticle-Mediated Immobilization. PloS One 8, e53419.
Kulkarni S, Abro B, Lasio MLD, Stoll J, Grange DK, He M (2020). Clinical and Pathological Features of a Newborn With Compound Heterozygous ANKS6 Variants. Pediatr Dev Pathol 23, 235–239.
Lažetić V, Fay DS (2017). Conserved Ankyrin Repeat Proteins and Their NIMA Kinase Partners Regulate Extracellular Matrix Remodeling and Intracellular Trafficking in Caenorhabditis Elegans. Genetics 205, 273–293.
Lažetić V, Joseph BB, Bernazzani SM, Fay DS (2018). Actin Organization and Endocytic Trafficking Are Controlled by a Network Linking NIMA-Related Kinases to the CDC-42-SID-3/ACK1 Pathway. PLoS Genetics 14, e1007313.
Li Y, Xu W, Makova S, Brueckner M, Sun Z (2023). Inactivation of Invs/Nphp2 in Renal Epithelial Cells Drives Infantile Nephronophthisis like Phenotypes in Mouse. eLife 12(March).
Liu Z, Fujii T, Nukazuka A, Kurokawa R, Suzuki M, Fujisawa H, Takagi S (2005). C. Elegans PlexinA PLX-1 Mediates a Cell Contact-Dependent Stop Signal in Vulval Precursor Cells. Dev Biol 282, 138–151.
Liu R, Liang Q-N, Du S-Q, Hu X-J, Ding Y (2016). The Crystal Structure of Red Fluorescent Protein TagRFP-T Reveals the Mechanism of Its Superior Photostability. Biochem Biophys Res Commun 477, 229–234.
Merzlyak EM, Goedhart J, Shcherbo D, Bulina ME, Shcheglov AS, Fradkov AF, Gaintzeva A, Lukyanov KA, Lukyanov S, Gadella TWJ& Chudakov DM (2007). Bright Monomeric Red Fluorescent Protein with an Extended Fluorescence Lifetime. Nat Methods 4, 555–557.
Mochizuki T, Saijoh Y, Tsuchiya K, Shirayoshi Y, Takai S, Taya C, Yonekawa H, Yamada K, Nihei H, Nakatsuji N, *et al.* (1998). Cloning of Inv, a Gene That Controls Left/right Asymmetry and Kidney Development. Nature 395, 177–181.
Morgan D, Turnpenny L, Goodship J, Dai W, Majumder K, Matthews L, Gardner A, Schuster G, Vien L, Harrison W, *et al.* (1998). Inversin, a Novel Gene in the Vertebrate Left-Right Axis Pathway, Is Partially Deleted in the Inv Mouse. Nat Genet 20, 149–156.
Muller HJ (1932). Further Studies on the Nature and Causes of Gene Mutations. Proc 6th Internat Congr Genet 1, 213–255.
Nakajima Y, Kiyonari H, Mukumoto Y, Yokoyama T (2018). The Inv Compartment of Renal Cilia Is an Intraciliary Signal-Activating Center to Phosphorylate ANKS6. Kidney Int 93, 1108–1117.
Nihongaki Y, Suzuki H, Kawano F, Sato M (2014). Genetically Engineered Photoinducible Homodimerization System with Improved Dimer-Forming Efficiency. ACS Chem Biol 9, 617–621.
Otto EA, Schermer B, Obara T, O'Toole JF, Hiller KS, Mueller AM, Ruf RG, Hoefele J, Beekmann F, Landau D, *et al.* (2003). Mutations in INVS Encoding Inversin Cause Nephronophthisis Type 2, Linking Renal Cystic Disease to the Function of Primary Cilia and Left-Right Axis Determination. Nat Genet 34, 413–420.
Otto EA, Trapp ML, Schultheiss UT, Helou J, Quarmby LM, Hildebrandt F (2008). NEK8 Mutations Affect Ciliary and Centrosomal Localization and May Cause Nephronophthisis. J Am Soc Nephrol 19, 587–592.
Pédelacq J-D, Cabantous S, Tran T, Terwilliger TC, Waldo GS (2006). Engineering and Characterization of a Superfolder Green Fluorescent Protein. Nat Biotechnol 24, 79–88.
Pettersen EF, Goddard TD, Huang CC, Meng EC, Couch GS, Croll TI, Morris JH, Ferrin TE (2021). UCSF ChimeraX: Structure Visualization for Researchers, Educators, and Developers. Protein Sci 30, 70–82.
Redemann S, Schloissnig S, Ernst S, Pozniakowsky A, Ayloo S, Hyman AA, Bringmann H (2011). Codon Adaptation-Based Control of Protein Expression in C. Elegans. Nat Methods 8, 250–252.
Schindelin J, Arganda-Carreras I, Frise E, Kaynig V, Longair M, Pietzsch T, Preibisch S, Rueden C, Saalfeld S, Schmid B, *et al.* (2012). Fiji: An Open-Source Platform for Biological-Image Analysis. Nat Methods 9, 676–682.
Schwarz H, Popp B, Airik R, Torabi N, Knaup KX, Stoeckert J, Wiech T, Amann K, Reis A, Schiffer M, *et al.* (2022). Biallelic ANKS6 Mutations Cause Late-Onset Ciliopathy with Chronic Kidney Disease through YAP Dysregulation. Hum Mol Gen 31, 1357–1369.
Scott DJ, Gunn NJ, Yong KJ, Wimmer VC, Veldhuis NA, Challis LM, Haidar M, Petrou S, Bathgate RAD, Griffin MDW (2018). A Novel Ultra-Stable, Monomeric Green Fluorescent Protein For Direct Volumetric Imaging of Whole Organs Using CLARITY. Sci Rep 8, 1–15.
Shaner NC, Lin MZ, McKeown MR, Steinbach PA, Hazelwood KL, Davidson MW, Tsien RY (2008). Improving the Photostability of Bright Monomeric Orange and Red Fluorescent Proteins. Nat Methods 5, 545–551.
Shemiakina II, Ermakova GV, Cranfill PJ, Baird MA, Evans RA, Souslova EA, Staroverov DB, Gorokhovatsky AY, Putintseva EV, Gorodnicheva TV, *et al.* (2012). A Monomeric Red Fluorescent Protein with Low Cytotoxicity. Nat Commun 3, 1204.
Shiba D, Manning DK, Koga H, Beier DR, Yokoyama T (2010). Inv Acts as a Molecular Anchor for Nphp3 and Nek8 in the Proximal Segment of Primary Cilia. Cytoskeleton 67, 112–119.
Shrode LB, Lewis ZA, White LD, Bell-Pedersen D, Ebbole DJ (2001). Vvd Is Required for Light Adaptation of Conidiation-Specific Genes of Neurospora Crassa, but Not Circadian Conidiation. Fungal Genet Biol 32, 169–181.
Simons M, Gloy J, Ganner A, Bullerkotte A, Bashkurov M, Krönig C, Schermer B, Benzing T, Cabello OA, Jenny A, *et al.* (2005). Inversin, the Gene Product Mutated in Nephronophthisis Type II, Functions as a Molecular Switch between Wnt Signaling Pathways. Nat Genet 37, 537–543.
Snapp EL, Hegde RS, Francolini M, Lombardo F, Colombo S, Pedrazzini E, Borgese N, Lippincott-Schwartz J (2003). Formation of Stacked ER Cisternae by Low Affinity Protein Interactions. J Cell Biol 163, 257–269.
Stolpner N, Dickinson DJ (2022). Single-Cell Single-Molecule Pull-Down (scSiMPull) for Detection of Protein Complexes from Embryonic Lysates. Methods Mol Biol 2438, 59–81.
Taskiran EZ, Korkmaz E, Gucer S, Kosukcu C, Kaymaz F, Koyunlar C, Bryda EC, Chaki M, Lu D, Vadnagara K, *et al.* (2014). Mutations in ANKS6 Cause a Nephronophthisis-like Phenotype with ESRD. J Am Soc Nephrol 25, 1653–1661.
Vaidya AT, Chen C-H, Dunlap JC, Loros JJ, Crane BR (2011). Structure of a Light-Activated LOV Protein Dimer That Regulates Transcription. Sci Signal 4, ra50.
Wannier TM, Gillespie SK, Hutchins N, Scott McIsaac R, Wu S-Y, Shen Y, Campbell RE, Brown KS, Mayo SL (2018). Monomerization of Far-Red Fluorescent Proteins. Proc Natl Acad Sci USA 115, E11294–E11301.
Yochem J, Lažetić V, Bell L, Chen L, Fay D (2015). C. Elegans NIMA-Related Kinases NEKL-2 and NEKL-3 Are Required for the Completion of Molting. Dev Biol 398, 255–266.
Yokoyama T, Copeland NG, Jenkins NA, Montgomery CA, Elder FFB, Overbeek PA (1993). Reversal of Left-Right Asymmetry: A Situs Inversus Mutation. Science 260, 679–682.
Zacharias DA, Violin JD, Newton AC, Tsien RY (2002). Partitioning of Lipid-Modified Monomeric GFPs into Membrane Microdomains of Live Cells. Science 296, 913–916.
Zalli D, Bayliss R, Fry AM (2012). The Nek8 Protein Kinase, Mutated in the Human Cystic Kidney Disease Nephronophthisis, Is Both Activated and Degraded during Ciliogenesis. Hum Mol Gen 21, 1155–1171.
Zhong Z, Yan X, Fang Z, Dong Y, Tan J, Xie J, Hu L, Zhang S, Qin W (2022). Case Report: Adolescent-Onset Isolated Nephronophthisis Caused by a Novel Homozygous Inversin Mutation. Front Genet 13(May), 847397.
Zoltowski BD, Crane BR (2008). Light Activation of the LOV Protein Vivid Generates a Rapidly Exchanging Dimer. Biochemistry 47, 7012–7019.